BIOCHEMISTRY
including biophysical chemistry & molecular biology
Article

Biochemistry **2010,** *49,* 8955–8966 8955
DOI: 10.1021/bi100988p

Secondary Structure and Solvent Accessibility of a Calmodulin-Binding C-Terminal Segment of Membrane-Associated Myelin Basic Protein†

Lopamudra Homchaudhuri,‡ Miguel De Avila,§ Stina B. Nilsson,§ Kyrylo Bessonov,§ Graham S. T. Smith,§ Vladimir V. Bamm,§ Abdiwahab A. Musse,§,|| George Harauz,§ and Joan M. Boggs*,‡

‡*Department of Molecular Structure and Function, Research Institute, Hospital for Sick Children, Toronto, Ontario, Canada, and Department of Laboratory Medicine and Pathobiology, University of Toronto, Toronto, Ontario, Canada, and* §*Department of Molecular and Cellular Biology, University of Guelph, 50 Stone Road East, Guelph, Ontario, Canada N1G 2W1*
||*Present address: Department of Biological Chemistry, David Geffen School of Medicine, University of California, Los Angeles, CA 90095-1737.*

Received June 18, 2010; Revised Manuscript Received September 8, 2010

ABSTRACT: Myelin basic protein (MBP), specifically the 18.5 kDa isoform, is a peripheral membrane protein and a major component of mammalian central nervous system myelin. It is an intrinsically disordered and multifunctional protein that binds cytoskeletal and other cytosolic proteins to a membrane surface and thereby acquires ordered structure. These associations are modulated by post-translational modifications of MBP, as well as by interactions of MBP with Ca^{2+}-calmodulin (CaM). Enzymatic deimination of usually six arginine residues to citrulline results in a decrease in the net positive charge of the protein from 19 to ≤13. This deiminated form is found in greater amounts in normal children and in adult patients with the demyelinating disease multiple sclerosis. In this paper, we examine the secondary structure of a calmodulin-binding domain, residues A141−L154, when associated with a lipid bilayer in recombinant murine 18.5 kDa forms rmC1 (unmodified) and rmC8 (pseudodeiminated). We demonstrate here by site-directed spin labeling and electron paramagnetic resonance (EPR) spectroscopy that the Y142−L154 segment in membrane-associated rmC1 forms an amphipathic α-helix, with high accessibility to O_2 and low accessibility to NiEDDA. In membrane-associated rmC8, this segment assumed a structure distorted from an α-helix. Spin-labeled residues in rmC1 in solution were more immobilized on binding Ca^{2+}-CaM than those in rmC8. Furthermore, rmC8 was dissociated more readily from a lipid bilayer by Ca^{2+}-CaM than was rmC1. These results confirm both a predicted induced ordering upon membrane association in a specific segment of 18.5 kDa MBP, and that this segment is a CaM-binding site, with both interactions weakened by deimination of residues outside of this segment. The deiminated form would be more susceptible to regulation of its membrane binding functions by Ca^{2+}-CaM than the unmodified form.

Myelin basic protein (MBP)[1] is a highly basic peripheral membrane protein and a major component of human central nervous system (CNS) myelin. It is the second most abundant protein in CNS myelin after proteolipid protein and accounts for 30% of the total protein content in myelin (*1*). The classic 18.5 kDa isoform of MBP, the major isoform in humans, is highly conserved in sequence in mammals (*2*) and occurs in the cytoplasmic leaflet of the oligodendrocyte, where it mediates myelin compaction by bringing together apposed cytoplasmic surfaces rich in acidic lipids (*3*, *4*). In *shiverer* mutant mice that carry deletions in the MBP gene that prevent expression of MBP, compact myelin in the CNS is lacking (*4*, *5*).

MBP is an intrinsically disordered protein that undergoes extensive post-translational modifications (*6*−*10*). Like other intrinsically disordered proteins, MBP assumes some ordered structure upon interacting with its binding partners, e.g., upon interacting with lipid membranes or proteins (*11*), albeit with a good deal of polymorphism, or "fuzziness", remaining (*12*). It has been shown by us previously, using the combination of site-directed spin labeling and electron paramagnetic resonance spectroscopy (SDSL−EPR), that a central segment of the protein (V83−T92) of recombinant murine 18.5 kDa MBP (rmMBP, with murine 18.5 kDa sequence numbering used henceforth unless otherwise indicated) forms an amphipathic α-helix upon association with lipid bilayers whose composition mimics that of the cytoplasmic leaflet of myelin (*13*). This structure was subsequently confirmed by solution NMR spectroscopy of a synthetic

†This work has been supported primarily by a grant to J.M.B. and G.H. from the Canadian Institutes of Health Research (CIHR MOP 86483) and a grant to G.H. from the Natural Sciences and Engineering Research Council of Canada (NSERC, Discovery Grant RG121541). L.H. and V.V.B. were the recipients of Postdoctoral Fellowships and A.A.M. and G.S.T.S. of Doctoral Studentships from the Multiple Sclerosis Society of Canada.

*To whom correspondence should be addressed: Department of Molecular Structure and Function, Research Institute, Hospital for Sick Children, 555 University Ave., Toronto, Ontario, Canada M5G 1X8. Phone: (416) 813-5919. Fax: (416) 813-5022. E-mail: jmboggs@sickkids.ca.

[1]Abbreviations: C1, most cationic charge component MBP; C8, least cationic charge component MBP; CaM, Ca^{2+}-calmodulin; CNS, central nervous system; Cyt-LUV, LUV with the lipid composition of the cytoplasmic monolayer of myelin; DMPC, dimyristoylphosphatidylcholine; DPPH, 1,1′-diphenyl-2-picrylhydrazyl; EAE, experimental allergic encephalomyelitis; EPR, electron paramagnetic resonance; HEPES, *N*-(2-hydroxyethyl)piperazine-*N*′-2-ethanesulfonic acid; LUV, large unilamellar vesicle; MBP, myelin basic protein; MS, multiple sclerosis; MTS-SL, [1-oxyl-2,2,5,5-tetramethyl-D-pyrroline-3-methyl] methanethiosulfonate spin-label; *n*-doxyl-PC, 1-palmitoyl-2-stearoyl(*n*-doxyl)-*sn*-glycero-3-phosphocholine; NiEDDA, nickel ethylenediaminediacetate; PAD2, peptidylarginine deiminase 2; PC, phosphatidylcholine; PE, phosphatidylethanolamine; PI, phosphatidylinositol; PS, phosphatidylserine; rmC1, recombinant murine C1 18.5 kDa MBP variant; rmC8, recombinant murine C8 18.5 kDa MBP variant; rmMBP, recombinant murine 18.5 kDa MBP; SDSL, site-directed spin labeling; SM, sphingomyelin; TEMPO, 2,2,6,6-tetramethylpiperidine-1-oxyl; TEMPO-PC, 1,2-dipalmitoyl-*sn*-glycero-3-phospho(TEMPO)choline; TPX, tetramethylpentene polymer.

Published on Web 09/10/2010

Q78−T95 peptide in association with dodecylphosphocholine micelles (*14*). Solution NMR spectroscopy has further shown that full-length 18.5 kDa rmMBP acquires some ordered transient secondary structure under membrane-mimetic conditions (*15*). This report identified two more segments in rmMBP, in addition to the segment mentioned above (V83−T92), viz., T33−D46 and Y142−L154, that can form transient amphipathic α-helices under membrane-mimetic conditions (*16*). This structure could thus potentially be stabilized by interaction with membranes and/or other proteins. One of the segments thus identified, Y142−L154, overlaps most of the predicted T147−D158 CaM-binding site of rmMBP (*15*).

MBP interacts with a large number of binding partners in vitro and is considered to be a multifunctional protein (*16*, *17*). It imparts structure to the myelin membrane, sequesters phosphoinositides, mediates cytoskeletal assembly, binds calmodulin in a Ca^{2+}-dependent manner, and binds SH3 domain-containing proteins (*16*−*24*). It also tethers cytoskeletal and SH3 domain-containing proteins to a membrane surface (*17*, *18*, *21*, *25*, *26*). Its level of colocalization with actin filaments increases on plasma membrane ruffles when MBP-transfected immortalized oligodendrocytes are stimulated with phorbol 12-myristate 13-acetate, an activator of the protein kinase C pathway (*27*). MBP also plays a role in transmembrane signal transmission and in axon−myelin communication (*1*, *17*, *28*). For example, the absence of MBP in the *shiverer* mouse mutant leads to a striking excess of axonal sodium channels despite contact of oligodendrocyte membranes with the axon, indicating that the presence of MBP in compact myelin downregulates axonal sodium channel density (*29*). The 18.5 kDa isoform of MBP has also been recently found to decrease the rate of Ca^{2+} influx into immortalized oligodendrocytes upon activation of voltage-gated calcium channels triggered by high concentrations of K^+ ions and could be responsible for maintaining relatively constant levels of Ca^{2+} within the cytoplasm of oligodendrocytes (*30*).

The numerous post-translational modifications that 18.5 kDa MBP undergoes include N-terminal acylation, deimination, deamidation, and phosphorylation (*6*−*10*). The diverse modifications result in the generation of a number of charge isomers or components of the protein, which are denoted C1−C8. These modifications of MBP modulate its interactions with lipid membranes and proteins such as actin, tubulin, and CaM (*16*, *17*). In this article, we focus on charge components C1 and C8. The C1 component is the least-modified, most cationic form of 18.5 kDa MBP (pI >10), whereas C8 is the most modified and least positively charged form due primarily to citrullination, which is the enzymatic deimination of six Arg residues (*8*, *31*, *32*). Deimination is catalyzed by a Ca^{2+}-dependent enzyme PAD2 (a member of the family of peptidylarginine deiminases) that is present in CNS white matter and also in oligodendrocytes (*32*). The relative proportion of modified MBP components appears to be regulated in myelin. Healthy adult myelin is characterized by a higher proportion of the C1 isomer, whereas the C8 isomer is found at elevated levels in early stages of myelination as well as in the white matter of patients suffering from the human autoimmune demyelinating disease multiple sclerosis (MS) (*33*, *34*). Membrane-associated rmC8 is hydrolyzed by cathepsin D 3 times faster than membrane-associated rmC1 (*35*). In particular, the V86−T95 segment of human 18.5 kDa MBP (identical to murine residues V83−T92) is a B-cell epitope and an important T-cell recognition site in human MBP (*36*). This primary immunodominant epitope has been shown to form a more highly surface-exposed and shorter amphipathic α-helix in rmC8 than in rmC1 and contains one of the Phe-Phe pairs cleaved by cathepsin D, explaining why rmC8 was more readily cleaved than rmC1 (*35*).

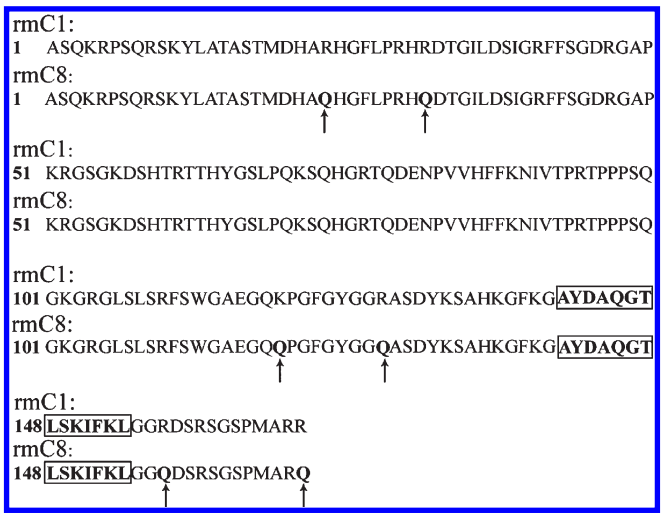

FIGURE 1: Amino acid sequences of recombinant murine 18.5 kDa MBP variants rmC1 (unmodified) and rmC8 (pseudodeiminated). The pseudodeiminated substitution sites are shown in boldface and denoted with arrows. The segment of interest in this paper, A141−L154, is enclosed in a black box.

In this paper, we examine the conformation and solvent accessibility of a C-terminal segment of membrane-associated rmMBP (A141−L154) in a myelin-mimetic lipid bilayer. This segment is a secondary immunodominant epitope (*36*) and overlaps a previously predicted primary CaM-binding domain (T147−D158) of rmMBP (*15*). We compare the natural C1 and C8 charge components using the respective recombinant murine forms, rmC1 and pseudodeiminated rmC8. In the latter variant, Gln is substituted with five Arg residues and one Lys residue (Figure 1) (*37*). The technique we use here is a combination of site-directed spin labeling (SDSL) and electron paramagnetic resonance (EPR) spectroscopy. EPR spectroscopy is a powerful tool for studying the association of proteins such as MBP with lipid membranes (*38*−*40*). The segment (Y142−L154) was previously reported to have the propensity to form an α-helix under membrane-mimetic conditions, as ascertained by solution NMR spectroscopy, and H^N−N chemical shifts of residues in this segment were shown to be the most affected upon interaction with CaM, indicating that this entire region may be involved in binding CaM (*15*). A helical wheel projection (Figure 2A,B) shows that this segment (A141−L154) is strongly amphipathic, although not as hydrophobic as the V83−T92 segment studied previously (*13*).

Our results show that on binding to a lipid bilayer, the Y142−L154 segment in rmC1 forms an amphipathic α-helix. However, the corresponding segment in rmC8 does not assume any ordered (i.e., periodic) secondary structure. Because this segment of the protein is also considered to be the primary CaM target, we have also mapped its specific Ca^{2+}-CaM interaction sites using SDSL−EPR. Binding to Ca^{2+}-CaM in solution causes more immobilization of residues A141−L154 in rmC1 than in rmC8. When the rmMBP variants are reconstituted with membranes, Ca^{2+}-CaM dissociates rmC8 more readily from the bilayer than rmC1.

MATERIALS AND METHODS

Materials. The lipids L-α-phosphatidylcholine (PC, egg), L-α-phosphatidylethanolamine (PE, porcine brain, contains 50%

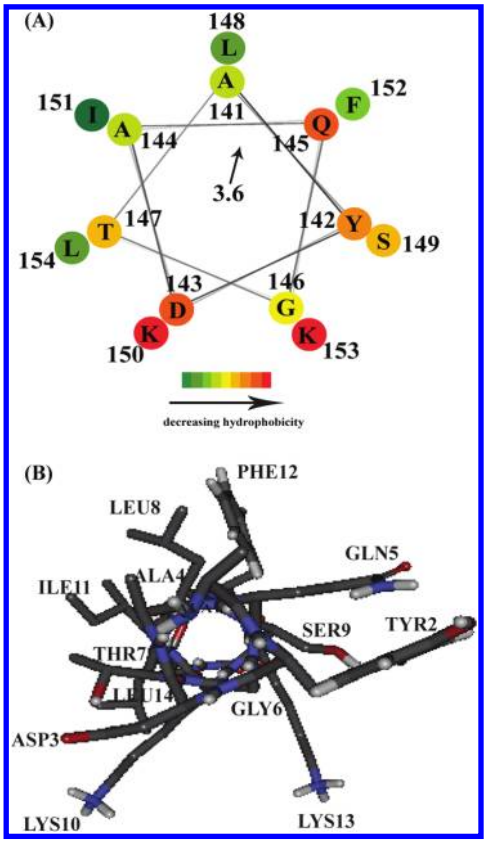

FIGURE 2: (A) Helical wheel representations of the A141−L154 segment of murine 18.5 kDa MBP created using the program accessible via http://rzlab.ucr.edu/scripts/wheel with a periodicity of 3.6 residues per turn. The residues are colored on the basis of hydrophobicity values predicted by the averaged Kyte−Doolittle hydrophobicity scale (*64*). The color scheme used varies from green (for hydrophobic residues) to red (for charged residues). Glycine, which has a hydrophobicity value of zero in this scale, is colored yellow. The arrow denotes the direction of the hydrophobic moment. (B) Side chains of the A141−L154 segment modeled in silico as an α-helical peptide using PeptideBuilder as described in Materials and Methods, displayed using Discovery Studio Visualizer version 2.5. The side chains are shown in stick representation with nitrogen atoms colored blue and oxygen atoms red.

plasmalogen form), L-α-phosphatidylserine (PS, porcine brain, Na^+ salt), L-α-phosphatidylinositol (PI, bovine liver, Na^+ salt), cholesterol, and sphingomyelin (SM, porcine brain) were purchased from Avanti Polar Lipids (Alabaster, AL). The depth calibration curves were obtained using the following spin-labeled lipids, also purchased from Avanti Polar Lipids: 1-palmitoyl-2-stearoyl(*n*-doxyl)-*sn*-glycero-3-phosphocholine for which $n = 5$, 7, 10, and 12 (5-doxyl PC, 7-doxyl PC, 10-doxyl PC, and 12-doxyl PC, respectively) and 1,2-dipalmitoyl-*sn*-glycero-3-phospho-(Tempo)choline with TEMPO (2,2,6,6-tetramethylpiperidine-1-oxyl) bound to the quaternary ammonium group (Tempo-PC). All the lipids were dissolved in chloroform at concentrations of 5−10 mg/mL.

The sulfhydryl-reactive spin-label [1-oxyl-2,2,5,5-tetramethyl-D-pyrroline-3-methyl] methanethiosulfonate spin-label (MTS-SL) was purchased from Toronto Research Chemicals (Toronto, ON). Calmodulin (bovine brain, desiccate) was purchased from Calbiochem (La Jolla, CA). The paramagnetic reagent NiEDDA was synthesized as previously described (*41*). All chemicals used were of reagent grade and were acquired from either Fisher Scientific (Fair Lawn, NJ) or Sigma-Aldrich (St. Louis, MO).

Preparation and Purification of Cysteine-Containing Variants of rmC1 and rmC8. Recombinant murine rmC1 expression and purification were conducted as described previously (*42*). The pseudodeiminated variant of murine MBP (rmC8) was generated from rmC1 by sequential site-directed mutations (R25Q, R33Q, K119Q, R127Q, R157Q, and R168Q, murine sequence numbering) using the QuikChange protocol (Stratagene, La Jolla, CA) as described previously (*37*). A Cys scan was done on both rmC1 and rmC8 to generate single-Cys variants corresponding to each of the residues in the segment of A141−L154 (murine sequence numbering). These new single-Cys-substituted variants were prepared and labeled with the sulfhydryl-reactive spin-label MTS-SL as described previously (*43*); the spin-label is termed R1 in the literature (*39*).

Preparation of Large Unilamellar Vesicles (LUVs). Aliquots of chloroform solutions of cholesterol, PE, PS, PC, SM, and PI were combined in a 44:23:13:11:3:2 mole ratio, which is characteristic of the cytoplasmic leaflet of myelin (*44*, *45*). A trace amount of [^{3}H]cholesterol was added to give a specific activity of 200000 dpm/10 μmol of lipid, and the solvent was rapidly evaporated in a stream of nitrogen at 37 °C and lyophilized overnight to yield a lipid film containing 1 mg (1.8 μmol) of lipid. The lipid film was then dispersed in 20 mM HEPES-NaOH buffer (pH 7.4) containing 10 mM NaCl and 1 mM EDTA at 40 °C (above the phase transition temperatures of each of the lipids in the mix), with vigorous vortexing (*45*). The resulting multilamellar vesicles were frozen and thawed approximately five or six times and then passed through a polycarbonate membrane ~18−19 times using a syringe extruder (Avanti Polar Lipids), yielding approximately 100 nm diameter cytoplasmic large unilamellar vesicles (Cyt-LUVs). The final lipid concentration was verified by counting [^{3}H]cholesterol. For distance calibration, the Cyt-LUVs also contained 0.2 mol % spin-labeled lipid and nonlabeled MBP (rmC1) added as described below (*13*).

Reconstitution of Spin-Labeled rmMBP Variants with Cyt-LUVs. Spin-labeled rmMBP (50 μg, 2.7 nmol) was added to 1 mg of Cyt-LUVs (3.6 μmol) and mixed gently. The resulting suspension was left at room temperature (20 °C) for 10 min to allow protein−lipid binding to proceed to completion. The sample was loosely pelleted by sedimentation at 1000*g* for 20 min at 4 °C in a Z400K benchtop centrifuge, and the pellet was used for EPR measurements. Samples for measurements in 20 mM NiEDDA were prepared via addition of the suspension of the spin-labeled rmMBP−Cyt-LUV aggregate to a dry film of NiEDDA (obtained by lyophilization of the required amount of the NiEDDA solution) so that the final concentration of NiEDDA in the sample was 20 mM. The sample was then frozen and thawed a minimum of five times and sedimented at 1000*g* for 20 min at 4 °C. Nonlabeled MBP (rmC1) was added at a similar concentration to Cyt-LUVs containing spin-labeled lipids for the determination of the calibration curve.

EPR Measurements of rmC1 and rmC8 Reconstituted with Cyt-LUVs. Electron paramagnetic resonance (EPR) measurements were taken at the X-band (9.6 GHz) on an Elexsys E500 continuous wave EPR spectrometer (Bruker Instruments Inc., Billerica, MA) equipped with a Bruker ER4123D resonator. Spectra were recorded with a modulation amplitude of 1 G. For the measurement of signal-averaged EPR spectra, the pellet of the spin-labeled MBP−Cyt-LUV aggregate was taken up in a 25 μL borosilicate capillary tube and one of its ends heat sealed. The tube was then spun at 4000*g* for an additional 15 min at 4 °C. The capillary tube containing the sample was then placed in a wider

bore quartz tube and that tube loaded into the EPR cavity (ER4123D) with the pellet centered in the cavity. The spectra were recorded at a power of 10 mW. Power saturation measurements were taken in air (20% O_2) and N_2 by taking up spin-labeled MBP−Cyt-LUV pellets into gas permeable polymethylpentene (TPX) capillary tubes (*41*). The tubes were sealed at the bottom with wax and loaded into the EPR cavity for measurements. The EPR cavity was purged with N_2 gas for 15 min prior to measurements in NiEDDA and N_2 alone.

Analysis of Power Saturation Data. Power saturation measurements were taken via variation of the microwave power from 0.25 to 100 mW to obtain saturation curves. These curves were then fitted to obtain a parameter $P_{1/2}$, the power at which the first-derivative EPR signal amplitude is half that of its unsaturated value (*46*). The $P_{1/2}$ values were measured for each of the samples in air, N_2, and NiEDDA. The values of the normalized accessibility parameter, Π, a measure of accessibility of spin-labels to the paramagnetic relaxation agents NiEDDA and air, were calculated using the following relationships

$$\Pi_{\mathrm{NiEDDA}} = \frac{(P_{1/2}^{\mathrm{NiEDDA}} - P_{1/2}^{\mathrm{N_2}})/\Delta H}{P_{1/2}^{\mathrm{DPPH}}/\Delta H^{\mathrm{DPPH}}}$$

$$\Pi_{\mathrm{air}} = \frac{(P_{1/2}^{\mathrm{air}} - P_{1/2}^{\mathrm{N_2}})/\Delta H}{P_{1/2}^{\mathrm{DPPH}}/\Delta H^{\mathrm{DPPH}}}$$

where ΔH is the peak-to-peak width of the central resonance line of the first-derivative EPR spectrum and was measured for each spin-labeled variant at a low microwave power (2.5 mW) in N_2; the values of $P_{1/2}^{\mathrm{DPPH}}$ and ΔH^{DPPH} were measured using a 1,1′-diphenyl-2-picrylhydrazyl (DPPH) standard prepared from a 1:10000 DPPH/KCl mixture (*41*). The depth parameter (or relative accessibility parameter) Φ was determined using the equation

$$\Phi = \ln\left(\frac{\Pi_{\mathrm{air}}}{\Pi_{\mathrm{NiEDDA}}}\right)$$

The depth parameters (Φ) of the spin-labeled proteins were then fitted to a lipid calibration curve to calculate their depths of penetration (in angstroms) into the lipid bilayer (*13*, *43*, *47*).

EPR Measurements of Spin-Labeled rmMBP−Ca^{2+}-CaM Mixtures. For binding to spin-labeled rmMBP, a Ca^{2+}-CaM solution was prepared in 10 mM HEPES-NaOH buffer, containing 250 mM NaCl and 1 mM $CaCl_2$, yielding a 10 mg/mL solution of protein. Spin-labeled rmC1 or rmC8 (2 nmol) was then combined with 4 nmol of Ca^{2+}-CaM in a final volume of 60 μL, and the solution was loaded into borosilicate capillary tubes for EPR measurements. The protein concentration of each spin-labeled rmMBP variant was determined using a modified bicinchoninic acid assay (*48*).

Assay of Ca^{2+}-CaM-Mediated Dissociation of MBP from the Membrane. For interaction with membrane-associated MBP, a Ca^{2+}-CaM solution was prepared in 10 mM HEPES-NaOH buffer (pH 7.4) containing 100 mM NaCl and 1 mM $CaCl_2$ (buffer A), yielding a protein concentration of 10 mg/mL (598 μM). Unlabeled rmC1 and rmC8 solutions were prepared at a final concentration of 0.85 mg/mL in the same buffer. Cyt-LUVs containing 1 mg (1.8 μmol) of lipids were prepared in 10 mM HEPES-NaOH buffer (pH 7.4) containing 100 mM NaCl (buffer B). Aliquots containing 50 μg (2.7 nmol) of rmC1 or rmC8 were added to 1 mg of Cyt-LUVs, followed by addition of 5.4 nmol of Ca^{2+}-CaM. The final volume of the suspension was increased to 500 μL using buffer A. The suspension was left for 30 min at room temperature (20 °C) and was then sedimented at 13000*g* for 30 min at 4 °C in a Z400K benchtop centrifuge. The supernatant was removed and the pellet resuspended in buffer A. Aliquots of the pellet and supernatant were then taken for counting [^{3}H]cholesterol, for protein assay by the Peterson method (*49*), and for gel electrophoresis on 10% Bis-Tris NuPAGE gels (Invitrogen, Mississauga, ON) along with standards of rmC1, rmC8, and calmodulin. Coomassie blue-stained gels were analyzed with a UVP image analyzer (UVP, Upland, CA), and band densities were compared to those of the standards to quantify the amount of protein in each sample (*25*). Band densities were within the linear range.

Molecular Dynamics Simulations of A141−L154 on a DMPC Bilayer. A molecular dynamics simulation of the interaction of the A141−L154 peptide alone with a pure lipid bilayer was performed using GROMACS version 4.0.5 (http://www.GROMACS.org/), run under a 32-bit Linux environment. The sequence NH_2-A^{141}YDAQGTLSKIFKL^{154}-COOH was modeled in silico as an α-helical peptide using PeptideBuilder (http://www.imtech.res.in/bvs/pepbuild/index.html). The N- and C-termini of the peptide were kept uncharged to prevent possible self-association of the ends. The membrane was a lipid bilayer of dimyristoylphosphatidylcholine (DMPC), using the publicly accessible DMPC structural coordinate file obtained from P. Tieleman's laboratory at the University of Calgary Biocomputing Group (http://moose.bio.ucalgary.ca/index.php?page=Structures and Topologies). To construct the simulation box, the peptide was first positioned just above this DMPC bilayer. The system was solvated with simple point charge water (spc 216) molecules added to both sides of the lipid bilayer, and an overall zero system charge was obtained via addition of counterions (sodium and chloride) to the aqueous layer. Energy minimization was first performed using the steepest descent algorithm. Molecular dynamics for 200 ns was performed using 96 processors on the SharcNet computer cluster (https://www.sharcnet.ca; total computation time of 3 weeks). For visualization of structural files and trajectories computed by GROMACS, Visual Molecular Dynamics (VMD) (http://www.ks.uiuc.edu/Research/vmd/) was extensively utilized. The secondary structure trajectory of the peptide was analyzed using the DSSP (Dictionary of Protein Secondary Structure) utility (*50*) incorporated into GROMACS.

RESULTS AND DISCUSSION

MBP binds to the negatively charged lipid bilayer using a combination of electrostatic and hydrophobic interactions, and additional attractive forces such as van der Waals interactions, or weak dipolar interactions between zwitterionic groups on lipid and MBP molecules (*43*, *51*). The net effect of these interactions causes hydrophobic side chains in MBP to penetrate deeper into the bilayer, compared to other residues that are stabilized at the interface by favorable interactions with the lipid headgroups (*13*).

In this paper, we study the secondary structure and solvent accessibility of the A141−L154 segment in rmC1 and rmC8, using spin-labeled single-cysteine substituted variants corresponding to each residue in the segment. Cysteine replacements were tolerated at all positions except at K150 in both rmC1 and rmC8. In both proteins, the K150C substitution and spin labeling caused them to aggregate. However, the rmC1 variants could be used immediately after preparation, and we have several data

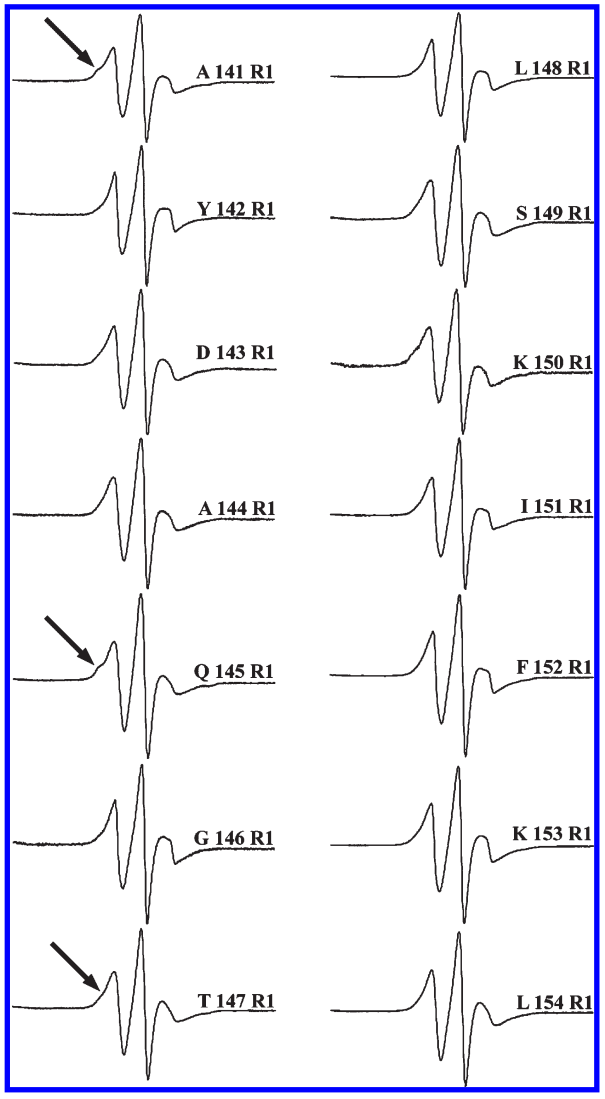

FIGURE 3: First-derivative EPR spectra of spin-labeled rmC1 reconstituted with Cyt-LUVs. The spectra of rmC8 variants were similar (not shown) although not identical to those of rmC1 as indicated by ΔH^{-1} values in Figure 4. The spectra were normalized to the amplitude of the central field line. The arrows denote the low field line of the spectral component indicative of motional restriction in the spectra of A141R1, Q145R1, and T147R1 in both rmC1 and rmC8.

points with rmC1-K150R1. The rmC8-K150C variant could not be purified in usable quantities at all. The fact that the conversion of Lys to Cys caused the protein to aggregate implies that this particular lysine residue is critical for the stability of the protein. Substitution of Cys at other positions [K153C and K88C (*13*)] did not destabilize either rmC1 or rmC8, indicating that it is not just the decrease in net charge that is responsible for the aggregation.

The first-derivative EPR spectra of all spin-labeled rmC1 and rmC8 variants were measured, and all exhibited narrow hyperfine lines (data not shown), indicating that the sites probed were not immobilized in solution (*52*). The spectra of spin-labeled proteins associated with Cyt-LUVs were broadened to varying degrees (shown for rmC1 in Figure 3; spectra of rmC8 were similar). The broadening of the hyperfine lines arises from hindered and anisotropic motion of the spin-labels when they are associated with lipids. In some cases (A141R1 and Q145R1), an additional broadened spectral component with larger hyperfine splitting was observed in both rmC1 and rmC8 (denoted with arrows in Figure 3). These spectral components were also

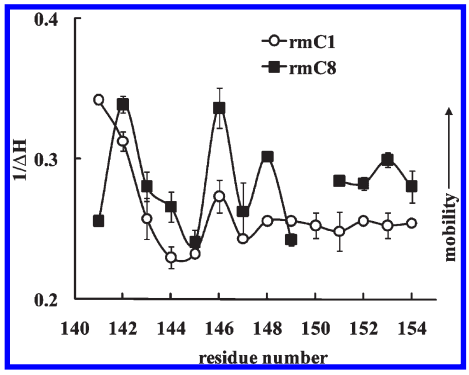

FIGURE 4: Plot of the inverse of the width (ΔH^{-1}) of the midfield line from first-derivative EPR spectra of spin-labeled rmC1 (○) and rmC8 (■) reconstituted with Cyt-LUVs as a function of residue number. The value of ΔH denotes the width of the $m_I = 0$ line. Increasing values of ΔH indicate hindered motion. The error bars indicate the error involved in measurement of the width of the midfield line. The variant rmC8-K150R1 could not be measured because of its aggregation in solution.

present to a lesser degree in the spectra of other single-Cys-substituted variants and denote populations of spin-labels that are motionally restricted, possibly by tertiary contact interactions with nearest neighbor side chains, and/or segmental motions (*53*).

Mobility of A141−L154 in Membrane-Associated rmC1 and rmC8. The mobilities of spin-labeled residues in membrane-associated rmC1 and rmC8 are compared in Figure 4. The mobility of each Cyt-LUV-bound spin-labeled variant was calculated via measurement of the inverse of the peak-to-peak width (ΔH^{-1}) of the central resonance line from its first-derivative EPR spectrum (*13*, *43*). The spin-labeled rmC8 variants were slightly more mobile than the spin-labeled rmC1 variants. This result reinforces earlier observations of increased mobility of several sites examined in rmC8 in the C-terminal half because of weakened electrostatic interactions of less positively charged rmC8 (+13 compared to +19 for rmC1) with the lipid bilayer (*43*).

Secondary Structure and Solvent Accessibility of A141−L154 in Membrane-Associated rmC1 and rmC8. We next examined the secondary structure and solvent accessibilities of spin-labels in the membrane-associated Cys-substituted variants of rmC1 and rmC8 using EPR power saturation measurements. The accessibility values of spin-labels for paramagnetic relaxation agents NiEDDA and O_2 (Π_{NiEDDA} and Π_{air}, respectively) were measured. The neutral polar metal complex NiEDDA partitions into the aqueous phase, whereas O_2 is hydrophobic and tends to partition into the hydrocarbon tail region of the bilayer or the hydrophobic core of a globular protein. Spin-labels that are more exposed to the aqueous phase encounter NiEDDA, and those in a hydrophobic environment encounter O_2. Panels A and B of Figure 5 show plots of accessibilities of membrane-associated, spin-labeled residues of rmC1 and rmC8 with NiEDDA (Π_{NiEDDA}) and air (Π_{air}) as functions of residue position, respectively. The accessibility parameters are out of phase with each other, indicating asymmetric exposure of residues A141−L154 to NiEDDA and O_2 (Table 1). Most of the residues in rmC1 are more accessible to O_2 than to NiEDDA (Figure 5A), indicating that these residues are within a hydrophobic environment. In rmC8, residues in the N-terminal half exhibit greater accessibility to O_2 than to NiEDDA, whereas most residues at the C-terminal end of rmC8 (Figure 5B) are more accessible to NiEDDA than to O_2.

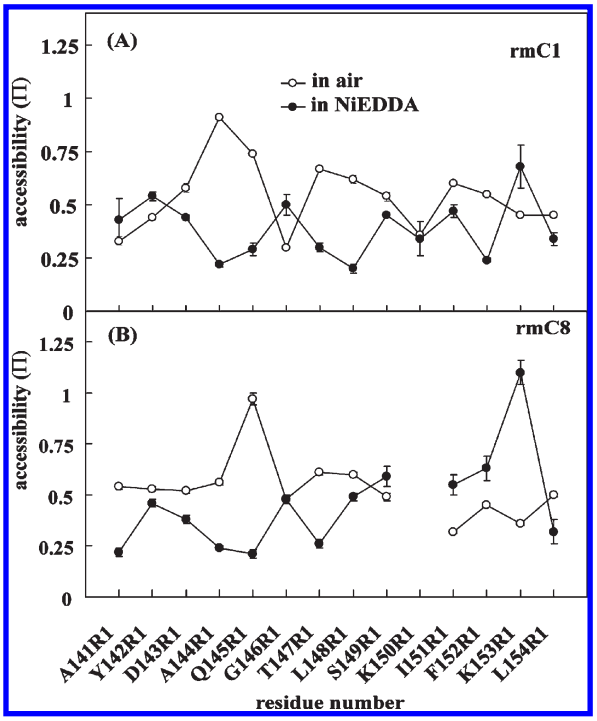

FIGURE 5: (A) Accessibility (Π) of spin-labeled rmC1 variants reconstituted with Cyt-LUVs to O_2 (air) (○) and NiEDDA (●), plotted as a function of residue number. (B) Accessibility (Π) of spin-labeled rmC8 variants bound to Cyt-LUVs to O_2 (air) (○) and NiEDDA (●), as a function of residue number. Results shown are averages over two sets of measurements, and the error bars indicate the range of the data. The variant rmC8-K150R1 could not be measured because of its aggregation in solution.

Table 1: Depth Parameters of rmCl and rmC8

spin-labeled MBP	Π_{air}	Π_{NiEDDA}	Φ	distance (Å)
rmC1-A141R1	0.33 ± 0.02	0.43 ± 0.10	−0.24 ± 0.16	9.04 ± 0.20
rmC8-A141R1	0.54 ± 0.01	0.22 ± 0.02	0.89 ± 0.05	10.5 ± 0.06
rmC1-Y142R1	0.44 ± 0.01	0.54 ± 0.02	−0.20 ± 0.01	9.09 ± 0.01
rmC8-Y142R1	0.53 ± 0.01	0.46 ± 0.02	0.015 ± 0.1	9.40 ± 0.2
rmC1-D143R1	0.58 ± 0.02	0.44 ± 0.01	0.27 ± 0.05	9.74 ± 0.06
rmC8-D143R1	0.52 ± 0.01	0.38 ± 0.02	0.30 ± 0.02	9.79 ± 0.03
rmC1-A144R1	0.91 ± 0.01	0.22 ± 0.01	1.39 ± 0.00	11.2 ± 0.05
rmC8-A144R1	0.56 ± 0.01	0.24 ± 0.01	0.84 ± 0.03	10.5 ± 0.04
rmC1-Q145R1	0.74 ± 0.01	0.29 ± 0.03	0.93 ± 0.07	10.6 ± 0.10
rmC8-Q145R1	0.97 ± 0.03	0.21 ± 0.02	1.55 ± 0.05	11.4 ± 0.09
rmC1-G146R1	0.30 ± 0.01	0.50 ± 0.05	−0.50 ± 0.06	8.65 ± 0.10
rmC8-G146R1	0.48 ± 0.01	0.48 ± 0.02	0.01 ± 0.02	9.39 ± 0.03
rmC1-T147R1	0.67 ± 0.01	0.30 ± 0.02	0.80 ± 0.06	10.4 ± 0.08
rmC8-T147R1	0.61 ± 0.01	0.26 ± 0.02	0.85 ± 0.05	10.5 ± 0.06
rmC1-L148R1	0.62 ± 0.02	0.20 ± 0.02	1.15 ± 0.05	10.9 ± 0.06
rmC8-L148R1	0.60 ± 0.01	0.49 ± 0.02	0.19 ± 0.02	9.64 ± 0.03
rmC1-S149R1	0.54 ± 0.02	0.45 ± 0.01	0.18 ± 0.02	9.61 ± 0.02
rmC8-S149R1	0.49 ± 0.02	0.59 ± 0.05	−0.18 ± 0.04	9.12 ± 0.05
rmC1-K150R1	0.36 ± 0.01	0.34 ± 0.08	0.06 ± 0.19	9.46 ± 0.30
rmC8-K150R1[a]				
rmC1-I151R1	0.60 ± 0.01	0.47 ± 0.03	0.24 ± 0.04	9.71 ± 0.06
rmC8-I151Rl	0.32 ± 0.01	0.55 ± 0.05	−0.54 ± 0.08	8.58 ± 0.1
rmC1-F152R1	0.55 ± 0.01	0.24 ± 0.01	0.81 ± 0.03	10.4 ± 0.04
rmC8-F152R1	0.45 ± 0.01	0.63 ± 0.06	−0.34 ± 0.08	8.89 ± 0.1
rmC1-K153R1	0.45 ± 0.01	0.68 ± 0.10	−0.40 ± 0.12	8.80 ± 0.20
rmC8-K153R1	0.36 ± 0.01	1.10 ± 0.06	−1.10 ± 0.00	7.58 ± 0.05
rmC1-L154R1	0.45 ± 0.01	0.34 ± 0.03	0.28 ± 0.06	9.75 ± 0.10
rmC8-L154R1	0.50 ± 0.01	0.32 ± 0.06	0.42 ± 0.04	9.95 ± 0.05
rmC8-S129Rl[b]	0.217 ± 0.01	3.02 ± 0.12	−2.64 ± 0.08	−5.02 ± 0.41[c]
Depth Parameters of Spin-Labeled PCs Used for the Calibration Curve				
TEMPO-PC	0.23	2.88	−2.53	−5
5-doxyl PC	0.18	0.41	−0.83	8.1
7-doxyl PC	0.29	0.12	0.84	10.5
10-doxyl PC	2.12	0.09	3.14	14
12-doxyl PC	2.67	0.06	3.80	16

[a]The variant rmC8-K150R1 aggregated and could not be used. [b]The variant rmC8-S129R1 was used as a control for comparison with previously published data (*43*). [c]Distance calculated using linear regression fit data for TEMPO-PC, 5-doxyl PC, and 7-doxyl PC.

The accessibility values listed in Table 1 were used to calculate the relative accessibility parameter, also called the depth parameter Φ. Plots of Φ values of spin-labeled rmC1 and rmC8 as functions of spin-label positions are shown in panels A and B of Figure 6, respectively. A positive value indicates a greater accessibility to oxygen than to NiEDDA, indicating that the residue is in a hydrophobic environment, whereas a negative value indicates that the residue is in a polar environment. Periodicity of accessibility parameters has been used extensively to predict secondary structures in both soluble and membrane proteins (*38*−*41*). The relative accessibility data for Cyt-LUV-bound rmC1 variants (Figure 6A) were fitted to a harmonic wave equation, and the calculated periodicity of the data points was 3.6 ± 0.11 residues per turn, indicating that the Y142−L154 segment in rmC1 indeed formed an α-helix under these conditions. The helix was slightly tilted at an angle of ~4° with respect to the plane of the lipid bilayer, with the N-terminal half in a more hydrophobic environment than the C-terminal half.

In contrast, the measured Φ values of the spin-labeled C-terminal segment of membrane-associated rmC8 (Figure 6B) could not be fitted reliably to a harmonic function, and this segment in rmC8 appeared to be distorted from an α-helical configuration. The gap in the plot of the rmC8 data set (Figure 6B) at residue K150 is due to excessive aggregation of this particular Cys-substituted variant as explained above. The N-terminal half of the A141−L154 segment in membrane-associated rmC8 is in a hydrophobic environment, similar to the corresponding segment in membrane-associated rmC1. However, the C-terminal part in membrane-associated rmC8 is in a more polar environment compared to that of the corresponding region in membrane-associated rmC1. The observed differences between rmC1 and rmC8 can be attributed to the replacement of Arg or Lys with Gln throughout the protein. Four of six such Lys or Arg to Gln replacements are located in the C-terminal half of MBP; the K119Q and R127Q mutations are located in the proximity of the N-terminus of the A141−L154 segment in rmC8, and one other replacement (R157Q) is located immediately downstream of this segment. The lack of periodic secondary structure of A141−L154, and the greater polarity of the environment of this segment's C-terminal half observed in membrane-associated rmC8, show the global effect of deimination of Arg residues in rmC8 on a specific region.

The Φ values for membrane proteins are generally interpreted in terms of penetration of the R1 side chain into the bilayer. The Φ values calculated here for each of the residues in the A141−L154 segment were used to calculate distances of penetration of each of the spin-labels into the bilayer (see Table 1). This calculation was done by fitting the Φ values of spin-labeled rmC1 and rmC8 to a lipid−MBP calibration curve (*47*) (data shown in Table 1), prepared using TEMPO-PC and a set of doxyl-labeled PCs as described previously (*13*, *43*). The distance (in angstroms) obtained from the lipid calibration curve indicates the distance from the nitrogen of the nitroxide spin-label to the lipid phosphate group. The calculated distances indicate that the spin-labeled

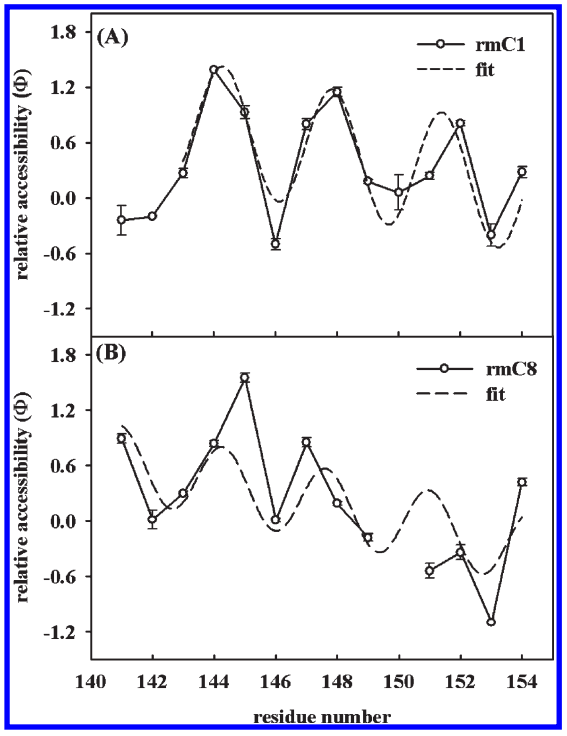

FIGURE 6: Plots of relative accessibility Φ of spin-labeled (A) rmC1 and (B) rmC8 variants, reconstituted with Cyt-LUVs, as a function of residue number, with measured data (○) and the fitted curve (– – –). The periodicity of the relative accessibility values was calculated by fitting the observed results to a tilted sine function, using Sigma Plot version 9.01. The results indicate averages of two sets of measurements, and the error bars indicate the range of the data. The variant rmC8-K150R1 could not be measured because of its aggregation in solution.

residues in membrane-associated rmC1 are in a hydrophobic environment sequestered deep in the bilayer (at depths of ≤11 Å) (Table 1). This degree of penetration seems unlikely because most of the residues, especially those in the N-terminal half of the segment, are not very hydrophobic. Residues A144R1, Q145R1, and T147R1 in both rmC1 and rmC8, and A141R1 in rmC8, had the highest Φ values, giving depths of penetration close to 11 Å (Table 1), according to this interpretation. This distance is longer than the depth of penetration determined for the V83−T92 segment, which is more hydrophobic (*13*, *35*). Repetition of this experiment with the previously studied variant rmC8-S129R1 with a solvent-exposed residue (*43*) indicated that S129R1 was in the aqueous phase (Table 1) as reported previously using a different spectrometer and calibration curve.

Molecular Dynamics Simulation of the A141−L154 Peptide on a DMPC Membrane. To visualize the behavior of this segment alone on the phospholipid bilayer, we performed a molecular dynamics simulation. The A141−L154 segment was modeled as an undistorted α-helix, positioned over a pure DMPC membrane in a hydrated environment, and the simulation was allowed to run for 200 ns. The peptide rapidly associated with the DMPC membrane as shown by the snapshot at 120 ns in Figure 7A. It is clear that the charged residues D143, K150, and K153 are less deeply buried in the bilayer than what was predicted from the distances calculated from the Φ values (> 8 Å) (refer to Table 1). According to Figure 7A, the COO^- moiety of residue D143 probes the bulk aqueous phase, whereas residues K150 and K153 are in a snorkeling orientation, with their ammonium moieties undergoing favorable interactions with the negatively charged phosphate groups in the lipid headgroup region (< 7 Å). The snorkeling of lysine residues has been observed in our earlier study involving the immunodominant V83−T92 segment of rmC1 (*13*), and lysine snorkeling in general maximizes the stability of a protein or peptide on a membrane. Figure 7A also shows that the hydrophobic residues I151, F152, and L154 penetrate deeper into the bilayer than the polar or charged residues. However, even these hydrophobic residues in the in silico peptide do not penetrate the bilayer as deeply as predicted from the calculated distances, though the latter distances were measured for the in situ full-length protein with a membrane that included negatively charged lipids (Table 1). Furthermore, the calculated distance of penetration is greater for the R1 side chains at the less hydrophobic N-terminal end of the A141−L154 segment than for those at the more hydrophobic C-terminal end, whereas the model predicts the opposite.

The precise disposition of the peptide with respect to the membrane changed naturally throughout the simulation, as there was also significant phospholipid motion (results not shown). An analysis of the peptide's secondary structure trajectory (*50*) showed that it remained primarily α-helical throughout the 200 ns simulation, except for some transient unraveling of the ends (Figure 7B). Although these molecular dynamics simulations could realistically be performed on only a small peptide fragment with a simplified lipid bilayer, the results nevertheless indicate that the modeled α-helical structure was stable, and that the natural relation of this amphipathic structure with respect to the membrane included hydrophobic interactions and lysine snorkeling. In the full-length protein, the α-helicity of rmC1 was experimentally demonstrated here, but the entire protein may have interacted with the membranes in a way that affected the environment of this particular segment on the lipid bilayer surface.

Causes of the Greater Hydrophobicity of the Environment of the C-Terminal Segment Compared to the Immunodominant Epitope. Therefore, on the basis of this result and the predicted amphipathicity of the A141−L154 segment (Figure 2A), we may conclude that the hydrophobic environment sampled by the residues in the C-terminal segment of both rmC1 and rmC8 is not just due to penetration of the side chains into the lipid bilayer. The 18.5 kDa MBP isoform is well-known to cause aggregation of negatively charged lipid vesicles because of adhesion of apposed bilayer surfaces (*17*, *45*), and hemifusion of the contacting monolayers of apposed vesicles (*54*). This close adhesion and/or hemifusion may explain the highly hydrophobic environment experienced by this segment. MBP-mediated bilayer adhesion may cause solvent exclusion and dehydration of the bilayer at these points, resulting in the greater solubility of O_2 and lower solubility of NiEDDA in the interbilayer space, thereby making the R1 side chains more accessible to O_2. This phenomenon could explain the high Φ values that were observed, which were larger than those obtained for the more hydrophobic V83−T92 segment. The middle region of MBP near the V83−T92 segment may not cause such close bilayer apposition because it is near a T^{92}PRTPPPS^{99} motif that can form a polyproline type II helix (*2*, *16*, *20*). Our ongoing molecular dynamics studies show a bend between the relatively stable α-helix and the polyproline type II helix for MBP in solution (cf. ref *55*). This structure in this segment of MBP may prevent close apposition of the bilayers associated with the central region of the MBP molecule (Figure 8), and thus, the bilayer surfaces in the vicinity of this central segment may be more hydrated compared

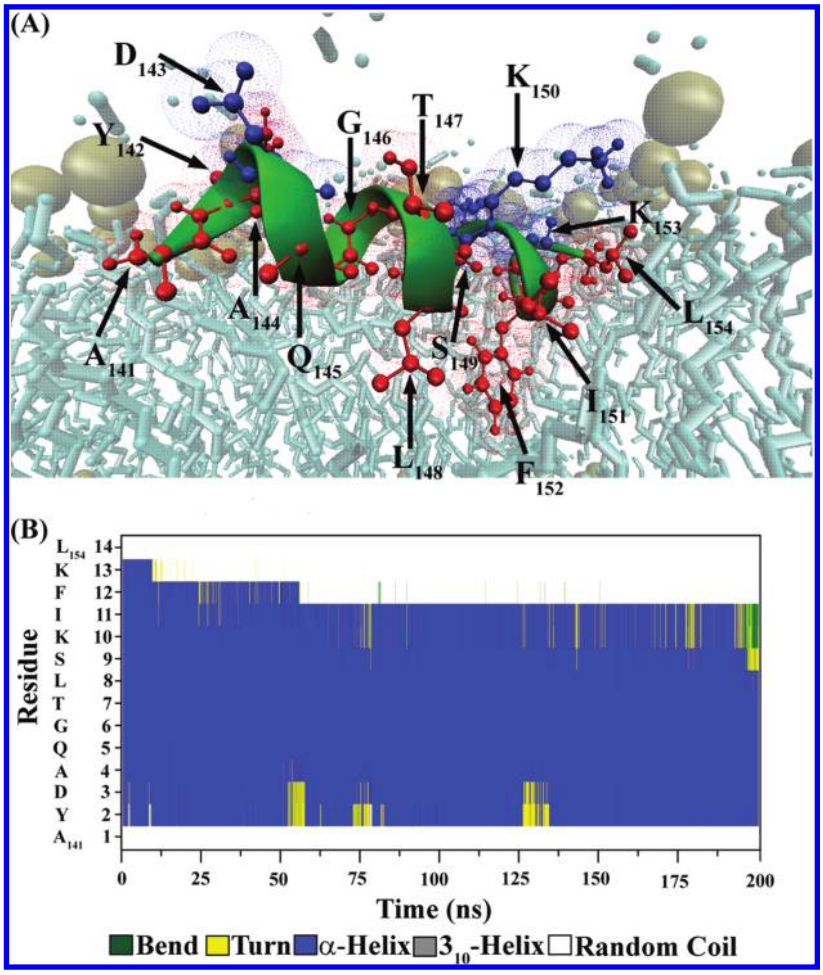

FIGURE 7: Molecular dynamics simulation of the A141−L154 segment on a DMPC membrane. (A) Snapshot of the simulation at 120 ns. The charged residues D143, K150, and K153 are colored blue. The remaining residues are colored red. (B) Secondary structure of each residue as a function of simulation time. The color blue indicates which residues form an α-helix with time up to 200 ns, with residues 1−14 corresponding to A141−L154, respectively. The helix at the C-terminal end unravels somewhat with time (the first and last terminal residues are always defined as "random coil" in this utility).

to those near the N- and C-terminal segments, which are more flexible (*56*) and may simultaneously bind to both apposed bilayers. Our earlier study of the environment of several residues distributed throughout the sequence of 18.5 kDa murine MBP showed that Ser44, adjacent to the Phe45-Phe46 pair, in the N-terminal segment was also in a very hydrophobic environment (*43*). Surprisingly, mutation of the Phe45-Phe46 pair to an Ala-Ala pair did not alter the hydrophobicity of its environment, in contrast to a similar mutation of the Phe86-Phe87 pair in the amphipathic helix of residues V83−T92. This result suggests that the hydrophobicity of the environment of S44R1 was also caused by its location in a dehydrated region between two apposed bilayers and supports our model depicted in Figure 8.

Interaction of rmC1 and rmC8 with Ca^{2+}-CaM. The 18.5 kDa MBP isoform interacts with CaM in a Ca^{2+}-dependent manner. Two CaM-binding sites have been suggested, especially for rmC8 (*24*, *57*−*60*). One of these has submicromolar affinity, most likely the Y142−L154 segment. Solution NMR spectroscopy has been used to demonstrate that rmC1 undergoes a marked conformational change upon binding to Ca^{2+}-CaM in solution (membrane-free), and that the Y142−L154 segment, which overlaps the predicted primary CaM-binding site of residues T147−D158, was most affected by the binding (*15*). However, the interaction of rmC8 with Ca^{2+}-CaM has not yet been examined by NMR spectroscopy.

Here, we used SDSL−EPR to map residues in the A141−L154 segment that are involved in the binding of rmC1 and rmC8 in solution with Ca^{2+}-CaM. Figure 9 shows first-derivative EPR spectra of 1:2 (mole ratio) mixtures of rmC1 and rmC8 with CaM in the presence of 1 mM Ca^{2+} ions. The combination of 1 mM Ca^{2+} and CaM immobilized some of the residues in the A141−L154 segments of both rmC1 and rmC8. A major broad spectral component with a large hyperfine splitting was observed in the low field region in the first-derivative EPR spectra of mixtures of rmC1 with Ca^{2+}-CaM and was accompanied by a minor sharp spectral component (Figure 9). The occurrence of the broad component indicates the presence of a population of spin-labeled side chains in rmMBP that are immobilized by tertiary contact with CaM (*52*, *53*, *61*). Most of the spin-labels in rmC8 variants were not significantly immobilized when compared with those in rmC1, except for A141R1 (Figure 9).

To quantify the extent of immobilization of each of the residues in the A141−L154 segments of rmC1 and rmC8, the ratio of the amplitude of the immobile component (I) (in the low field region) to the peak-to-peak amplitude of the central hyperfine line (M) was calculated. A plot of this ratio in rmC1 and rmC8 as a function of residue number is shown in Figure 10A. The relative I:M ratios are plotted as a function of residue number in Figure 10B. These relative I:M values were calculated by dividing the I:M ratio of each spin-labeled protein by the I:M

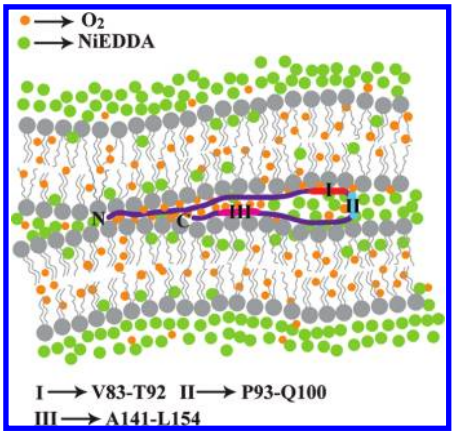

FIGURE 8: Schematic representation of 18.5 kDa MBP with its N- and C-terminal segments mediating close apposition of two phospholipid bilayers. Paramagnetic reagents, NiEDDA and O_2, are indicated by large green circles and smaller gold circles, respectively. The V83−T92 (I) (primary immunodominant epitope) [studied previously (*13*)], P93−Q100 (II) [which forms a potential bend and a polyproline helix (*20*, *55*)], and A141−L154 (III) (secondary immunodominant epitope, and part of the primary calmodulin binding segment) segments are colored red, blue, and magenta, respectively. S44R1 in the N-terminal region was shown earlier to be in a very hydrophobic environment and not affected by mutation of the adjacent F45-F46 pair to an A-A pair (*43*). The tight apposition of the bilayers by the N- and C-terminal segments results in solvent exclusion and makes their environment apolar with increased solubility of O_2 and decreased solubility of NiEDDA in this region, whereas the conformation of the P93−Q100 segment keeps the bilayers farther apart at this point, allowing greater hydration, an increased concentration of NiEDDA, and a decreased concentration of O_2.

ratio of the most immobilized residue for rmC1 and rmC8. Examination of Figure 10A shows that the spin-labels in the A141−L154 segment of rmC1 were more immobilized than the corresponding residues in rmC8, upon interaction with Ca^{2+}-CaM. In rmC1, there was a significant immobilized component for most of the residues along the entire A141−L154 segment, except for the two residues at its N-terminal end (A141 and Y142), and two residues at its C-terminal end (K153 and L154), which were more mobile. A different pattern of immobilization was seen for rmC8, where the N-terminal half of the spin-labeled segment was more immobilized than the C-terminal half (Figure 10B). In rmC1, residues Q145R1 and F152R1 were the most immobilized, followed by D143R1 and T147R1. In rmC8, residue A141R1 was the most immobilized, followed by D143R1 and T147R1.

Our previous studies using solution NMR spectroscopy of rmC1 revealed that residue T147, along with residues G155, G156, and G162, exhibited abnormally large chemical shifts upon interacting with Ca^{2+}-CaM (*15*). Our data here on the A141−L154 segment also show that T147R1 is significantly immobilized in rmC1 in the complex (Figure 9A). Independent studies of the structure of CaM when complexed with full-length MBP, and also with C-terminal peptides of MBP, were reported recently (*60*, *62*). The conclusions from both investigations point to Ca^{2+}-CaM having an elongated structure in these complexes. Solution NMR spectroscopy shows that MBP binds preferentially to the C-terminal lobe of CaM but has weak interactions with the central helix and the N-terminal lobe in CaM (*60*). The residues most affected in CaM include basic residues like R106 and K148, which may explain the immobilization of residues D143R1 and Q145R1 in the rmMBP−Ca^{2+}-CaM complexes observed here.

Both rmC1 and rmC8 are believed to be virtually fully bound to CaM under the conditions used, as the MBP concentration is

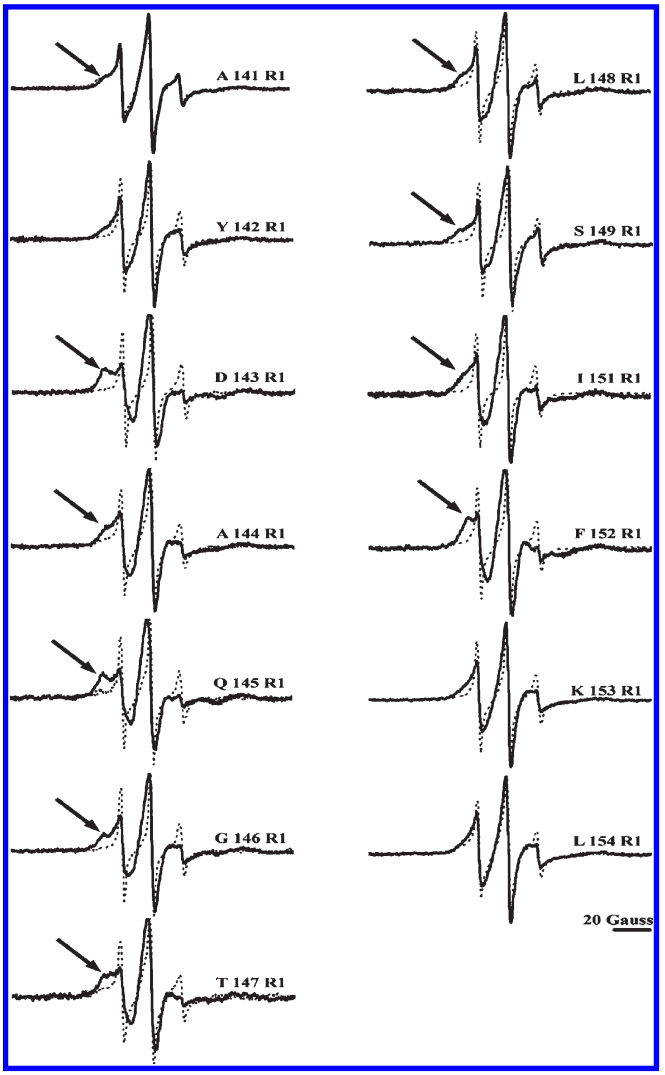

FIGURE 9: Normalized first-derivative EPR spectra of 1:2 (mole ratio) mixtures of rmMBP and Ca^{2+}-CaM in solution. The spectra were normalized relative to the amplitude of the central field line. The spectra of rmC8 variants (···) have been overlaid on the spectra of rmC1 variants (—). Arrows indicate the low field peak of a spectral component with larger hyperfine splitting indicative of motional restriction, because of tertiary contacts of MBP with Ca^{2+}-CaM. The variants rmC1-K150R1 and rmC8-K150R1 could not be measured because of their aggregation in solution.

33 μM, well above the reported K_d value of 0.14 μM for rmC1 (*24*, *62*). Several spin-labeled residues elsewhere in the protein were equally immobilized in rmC8 and rmC1 (*61*). Therefore, the significantly higher mobility of spin-labels in the A141−L154 segment in rmC8 compared to rmC1 (Figures 9 and 10A) may arise because of weaker interaction of this segment in rmC8 with Ca^{2+}-CaM. The higher mobility of residues in the C-terminal half of rmC8 compared to the N-terminal half may also be explained in terms of results reported from molecular docking simulations of the T147−D158 peptide on Ca^{2+}-CaM. These in silico studies showed that the deiminated peptide penetrates the CaM-binding tunnel with its C-terminus in a "forward" orientation, whereas the unmodified rmC1 peptide can penetrate the CaM-binding tunnel in either orientation, with both orientations being favorable in terms of docking energy (*61*, *63*). This result may explain why both the N- and C-terminal halves of this segment were immobilized in rmC1, in contrast with rmC8 in which spin-labels in the N-terminal half were preferentially immobilized.

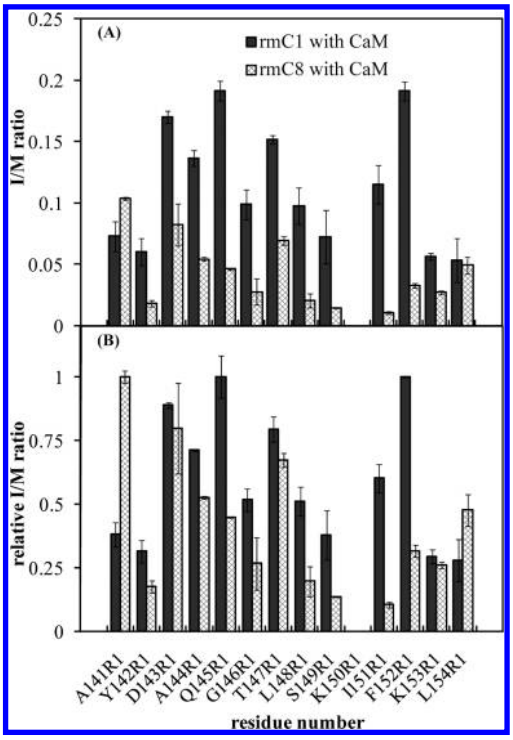

FIGURE 10: (A) Plot of the I:M ratio of the peak heights of the low field peak of the immobilized spectral component (I) and the peak-to-peak amplitude of the center field line (M) for spin-labeled rmC1 (black bars) and rmC8 (hatched bars), in the presence of CaM and 1 mM $CaCl_2$, as a function of spin-labeled residue number. The molar rmMBP:CaM ratio was 1:2. Data represent averages over two sets of measurements, and the error bars indicate the range. The variants rmC1-K150R1 and rmC8-K150R1 could not be measured because of their aggregation in solution. (B) Relative I:M ratios (calculated from values in panel A) plotted as a function of spin-labeled residue number. These relative ratios are used here to compare the relative immobilization of residues in rmC1 and rmC8, as compared to the most immobilized residue in each of these variants and the distribution of immobilized residues. The ratios are calculated separately for rmC1 and rmC8. The black bars indicate data for spin-labeled rmC1 variants; hatched bars denote data for spin-labeled rmC8 variants.

It is also possible that rmC8 adopts a different conformation on binding to Ca^{2+}-CaM than rmC1.

Interaction of Membrane-Bound MBP with Ca^{2+}-CaM. Ca^{2+}-CaM was shown earlier to bind to membrane-associated C1 (natural bovine 18.5 kDa MBP) and dissociate it from the lipid bilayer (*25*). Because the results presented here show that, in solution, the primary CaM-binding segment of spin-labeled rmC8 does not bind as well to CaM as in rmC1, we compared the ability of Ca^{2+}-CaM to interact with membrane-associated rmC1 and rmC8 and to dissociate them from the bilayer. Figure 11 shows a plot of the percentage of rmC1 and rmC8 bound to Cyt-LUVs before and after addition of Ca^{2+}-CaM. We observed that in the absence of Ca^{2+}-CaM, there is no significant difference in the amount of rmC1 (91%) or rmC8 (84%) bound to Cyt-LUVs. However, upon addition of Ca^{2+}-CaM, there is a marked drop in the levels of both rmC1 and rmC8 bound to the membrane, and the percentage of Cyt-LUV-bound rmC8 (21%) was much lower than that of Cyt-LUV-bound rmC1 (40%). Thus, Ca^{2+}-CaM dissociated rmC8 from the membrane twice as efficiently as rmC1, even though our results here for the interaction of the spin-labeled MBP components with Ca^{2+}-CaM in solution indicated that Ca^{2+}-CaM does not bind this segment of rmC8 as well as that in rmC1. However, Ca^{2+}-CaM may also

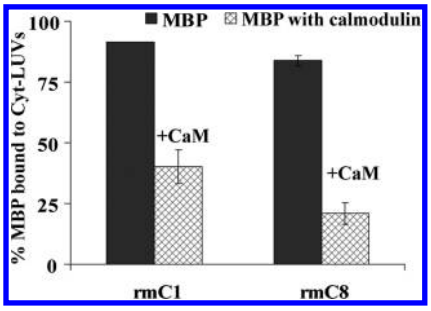

FIGURE 11: Percentages of unlabeled rmC1 and unlabeled rmC8 bound to Cyt-LUVs before (black bars) and after (hatched bars) treatment with Ca^{2+}-CaM. The rmMBP:CaM molar ratio was 1:2. Data represent the means of two independent experiments, and the error bars show the range.

bind to another segment of rmC8 (*24*, *57*−*60*) and thus dissociate the entire protein molecule from the membrane. Furthermore, the greater level of dissociation of rmC8 from the bilayer by Ca^{2+}-CaM may indicate weaker binding of pseudodeiminated rmC8 to the lipid bilayer, and/or greater exposure of some of its segments to the aqueous milieu, as shown here for the C-terminal end of the A141−L154 segment, and previously for the V83−T92 segment (*35*).

The greater level of dissociation of rmC8 from the bilayer by Ca^{2+}-CaM has important implications for the function of deiminated component C8 in oligodendrocytes or myelin in children, where it is elevated, and for the putative role of MBP in autoimmune response observed in MS, where elevated levels of C8 are also observed in adult CNS myelin. These results, in concert with our past report of more facile cleavage of membrane-associated rmC8 by cathepsin D (*35*), support our earlier conclusion that the membrane-associated form of the deiminated isomer is more accessible to the aqueous phase in lipid bilayers and to the cytoplasm, and hence to cytoplasmic proteins and enzymes in myelin or oligodendrocytes. The accessibility of membrane-associated C8 in myelin or oligodendrocytes to cytoplasmic proteins such as Ca^{2+}-CaM, which is also present in compact myelin (*60*), may result in MBP being dissociated from the membrane into the cytoplasm where degradative enzymes can hydrolyze the protein, releasing peptides that may trigger or sustain the immune response. Dissociation of C8 from the membrane by Ca^{2+}-CaM would also weaken its ability to tether cytoskeletal and signaling proteins to the membrane (*21*, *25*, *26*) and its ability to behave as a PIP_2-modulin [i.e., a $PI(4,5)P_2$-sequestering protein] (*22*). As we have just shown, Ca^{2+}-CaM also binds rmC1 associated with a lipid bilayer, dissociating it from the bilayer (though to a lesser extent than rmC8), and because CaM is present in compact myelin and shows some colocalization with MBP (*60*), it may modulate the binding of MBP to the myelin membrane in compact myelin and regulate other processes mediated by MBP.

CONCLUSIONS

Using spin-labeled single-cysteine variants of 18.5 kDa rmMBP, we have shown that the Y142−L154 segment in membrane-associated rmC1 forms an amphipathic α-helix with one side in a more hydrophobic environment than the other side. However, both sides are in a more hydrophobic environment (with a polarity gradient) than expected, as found earlier for S44R1 in the N-terminal region even after the mutation of the F45-F46 pair to an A-A pair (*43*). This result suggests that the N- and

C-terminal segments of MBP mediate close apposition of membrane surfaces, causing these segments to be dehydrated. The hydrophobic side of the Y142−L154 helix is next to the bilayer, with some side chains embedded in the bilayer and with the more polar side in the dehydrated space between the bilayers. This close bilayer adhesion mediated by the ends of the protein contrasts with that near a more central region of the molecule, which comprises the α-helical V83−T92 segment reported previously (*13*, *35*), followed by a polyproline type II helix domain (*2*, *20*). A bend may form in this central section of the molecule (*55*), thereby keeping the bilayers separated and better hydrated at this point. We also observed that the periodicity of the environment of residues in the A141−L154 segment of membrane-associated rmC8 appears to be distorted from an α-helical configuration, even though many of its residues are also sequestered in a hydrophobic environment. In addition, the C-terminal part of the A141−L154 segment is in a more polar environment than in rmC1. Less tight binding of the C-terminal half of rmC8, which contains four of the six Cit substitutions, may prevent this particular segment from adopting an ordered structure on association with lipids or causing equally tight adhesion of apposed bilayers as rmC1 (*8*). This effect of pseudodeimination elsewhere in the rmC8 sequence shows the effect of modifications of the protein, with resultant global conformational changes, on this segment. We have also shown here that almost all the residues in the A141−L154 segment of rmC1 are immobilized by the interaction with Ca^{2+}-CaM in solution. In contrast, the corresponding residues in rmC8 are immobilized to a lesser extent, which may be caused by the reduced affinity of the C-terminal end of MBP for CaM induced by the loss of net positive charge of the protein, or by a conformational change in rmC8. Ca^{2+}-CaM dissociates rmC8 from the membrane twice as efficiently as rmC1. Deimination may, therefore, make membrane-associated MBP more accessible to cytosolic proteins like Ca^{2+}-CaM, causing its dissociation from the membrane and exposure to enzymes that can cleave it. This process would generate MBP peptides that could cause or sustain an autoimmune response in MS. Furthermore, the increased level of dissociation of the deiminated form from the bilayer by Ca^{2+}-CaM would weaken the ability of MBP to adhere to the cytosolic surfaces of myelin and to act as a scaffolding protein that tethers other proteins to the membrane, thus affecting its function in normal oligodendrocytes and myelin.

ACKNOWLEDGMENT

We are grateful to Dr. Jun Liu (Department of Medical Genetics, University of Toronto) for kindly permitting us to use the Elexsys E500 EPR spectrometer and to Mr. Eoin Coll and Dr. Peter Tieleman (Department of Biological Sciences, University of Calgary, Calgary, AB) for generous assistance and guidance with the molecular dynamics simulations.

REFERENCES

1. Boggs, J. M. (2008) Myelin Basic Protein, Nova Science Publishers, Hauppauge, NY.
2. Harauz, G., and Libich, D. S. (2009) The classic basic protein of myelin: Conserved structural motifs and the dynamic molecular barcode involved in membrane adhesion and protein-protein interactions. *Curr. Protein Pept. Sci. 10*, 196–215.
3. Omlin, F. X., Webster, H. D., Palkovits, C. G., and Cohen, S. R. (1982) Immunocytochemical localization of basic protein in major dense line regions of central and peripheral myelin. *J. Cell Biol. 95*, 242–248.
4. Readhead, C., Takasashi, N., Shine, H. D., Saavedra, R., Sidman, R., and Hood, L. (1990) Role of myelin basic protein in the formation of central nervous system myelin. *Ann. N.Y. Acad. Sci. 605*, 280–285.
5. Privat, A., Jacque, C., Bourre, J. M., Dupouey, P., and Baumann, N. (1979) Absence of the major dense line in myelin of the mutant mouse "shiverer". *Neurosci. Lett. 12*, 107–112.
6. Chou, F. C., Chou, C. H., Shapira, R., and Kibler, R. F. (1976) Basis of microheterogeneity of myelin basic protein. *J. Biol. Chem. 251*, 2671–2679.
7. Zand, R., Li, M. X., Jin, X., and Lubman, D. (1998) Determination of the sites of posttranslational modifications in the charge isomers of bovine myelin basic protein by capillary electrophoresis-mass spectroscopy. *Biochemistry 37*, 2441–2449.
8. Wood, D. D., and Moscarello, M. A. (1989) The isolation, characterization, and lipid-aggregating properties of a citrulline containing myelin basic protein. *J. Biol. Chem. 264*, 5121–5127.
9. Zand, R., Jin, X., Kim, J., Wall, D. B., Gould, R., and Lubman, D. M. (2001) Studies of posttranslational modifications in spiny dogfish myelin basic protein. *Neurochem. Res. 26*, 539–547.
10. Moscarello, M. A., Pang, H., Pace-Asciak, C. R., and Wood, D. D. (1992) The N terminus of human myelin basic protein consists of C2, C4, C6, and C8 alkyl carboxylic acids. *J. Biol. Chem. 267*, 9779–9782.
11. Harauz, G., Ishiyama, N., Hill, C. M. D., Bates, I. R., Libich, D. S., and Farès, C. (2004) Myelin basic protein: Diverse conformational states of an intrinsically unstructured protein and its roles in myelin assembly and multiple sclerosis. *Micron 35*, 503–542.
12. Libich, D. S., Ahmed, M. A. M., Zhong, L., Bamm, V. V., Ladizhansky, V., and Harauz, G. (2010) Fuzzy complexes of myelin basic protein: NMR spectroscopic investigations of a polymorphic organizational linker of the central nervous system. *Biochem. Cell Biol. 88*, 143–155 (Special Issue on Protein Folding: Principles and Diseases).
13. Bates, I. R., Feix, J. B., Boggs, J. M., and Harauz, G. (2004) An immunodominant epitope of myelin basic protein is an amphipathic α-helix. *J. Biol. Chem. 279*, 5757–5764.
14. Farès, C., Libich, D. S., and Harauz, G. (2006) Solution NMR structure of an immunodominant epitope of myelin basic protein. Conformational dependence on environment of an intrinsically unstructured protein. *FEBS J. 273*, 601–614.
15. Libich, D. S., and Harauz, G. (2008) Backbone dynamics of the 18.5 kDa isoform of myelin basic protein reveals transient α-helices and a calmodulin-binding site. *Biophys. J. 94*, 4847–4866.
16. Harauz, G., Ladizhansky, V., and Boggs, J. M. (2009) Structural polymorphism and multifunctionality of myelin basic protein. *Biochemistry 48*, 8094–8104.
17. Boggs, J. M. (2006) Myelin basic protein: A multifunctional protein. *Cell. Mol. Life Sci. 63*, 1945–1961.
18. Boggs, J. M., Rangaraj, G., Gao, W., and Heng, Y. M. (2006) Effect of phosphorylation of myelin basic protein by MAPK on its interactions with actin and actin binding to a lipid membrane *in vitro*. *Biochemistry 45*, 391–401.
19. Rosetti, C. M., and Maggio, B. (2007) Protein-induced surface structuring in myelin membrane monolayers. *Biophys. J. 93*, 4254–4267.
20. Polverini, E., Rangaraj, G., Libich, D. S., Boggs, J. M., and Harauz, G. (2008) Binding of the proline-rich segment of myelin basic protein to SH3-domains: Spectroscopic, microarray, and modelling studies of ligand conformation and effects of post-translational modifications. *Biochemistry 47*, 267–282.
21. Homchaudhuri, L., Polverini, E., Gao, W., Harauz, G., and Boggs, J. M. (2009) Influence of membrane surface charge and post-translational modifications to myelin basic protein on its ability to tether the Fyn-SH3 domain to a membrane *in vitro*. *Biochemistry 48*, 2385–2393.
22. Musse, A. A., Gao, W., Homchaudhuri, L., Boggs, J. M., and Harauz, G. (2008) Myelin basic protein as a "PI(4,5)P2-modulin": A new biological function for a major central nervous system protein. *Biochemistry 47*, 10372–10382.
23. Galiano, M. R., Andrieux, A., Deloulme, J. C., Bosc, C., Schweitzer, A., Job, D., and Hallak, M. E. (2006) Myelin basic protein functions as a microtubule stabilizing protein in differentiated oligodendrocytes. *J. Neurosci. Res. 84*, 534–541.
24. Libich, D. S., Hill, C. M. D., Bates, I. R., Hallett, F. R., Armstrong, S., Siemiarczuk, A., and Harauz, G. (2003) Interaction of the 18.5-kD isoform of myelin basic protein with Ca^{2+}-calmodulin: Effects of deimination assessed by intrinsic Trp fluorescence spectroscopy, dynamic light scattering, and circular dichroism. *Protein Sci. 12*, 1507–1521.

25. Boggs, J. M., and Rangaraj, G. (2000) Interaction of lipid-bound myelin basic protein with actin filaments and calmodulin. *Biochemistry 39*, 7799–7806.
26. Boggs, J. M., Rangaraj, G., Hill, C. M. D., Bates, I. R., Heng, Y. M., and Harauz, G. (2005) Effect of arginine loss in myelin basic protein, as occurs in its deiminated charge isoform, on mediation of actin polymerization and actin binding to a lipid membrane *in vitro*. *Biochemistry 44*, 3524–3534.
27. Smith, G. S. T., Petley-Ragan, L. M., Gao, W., Boggs, J. M., and Harauz, G. (2010) Classic isoforms of myelin basic protein associate with the cytoskeleton in oligodendroglial cells during ruffling. Transactions of the American Society for Neurochemistry 41st Annual Meeting, OP05-01, American Society for Neurochemistry, Windermere, FL.
28. Dyer, C. A., Philibotte, T. M., Wolf, M. K., and Billings-Gagliardi, S. (1994) Myelin basic protein mediates extracellular signals that regulate microtubule stability in oligodendrocyte membrane sheets. *J. Neurosci. Res. 39*, 97–107.
29. Noebels, J. L., Marcom, P. K., and Jalilian-Tehrani, M. H. (1991) Sodium channel density in hypomyelinated brain increased by myelin basic protein gene deletion. *Nature 352*, 431–434.
30. Paez, P. M., Smith, G. S. T., Spreuer, V., Boggs, J. M., Harauz, G., Campagnoni, C. W., and Campagnoni, A. T. (2010) Classic 18.5 and 21.5 kDa isoforms of myelin basic protein inhibit calcium influx into oligodendroglial cells, in contrast to golli isoforms. Transactions of the American Society for Neurochemistry 41st Annual Meeting, PTW02-05, American Society for Neurochemistry, Windermere, FL.
31. Kim, J. K., Mastronardi, F. G., Wood, D. D., Lubman, D. M., Zand, R., and Moscarello, M. A. (2003) Multiple sclerosis: An important role for post-translational modifications of myelin basic protein in pathogenesis. *Mol. Cell. Proteomics 2*, 453–462.
32. Lamensa, J. W., and Moscarello, M. A. (1993) Deimination of human myelin basic protein by a peptidylarginine deiminase from bovine brain. *J. Neurochem. 61*, 987–996.
33. Moscarello, M. A., Wood, D. D., Ackerley, C., and Boulias, C. (1994) Myelin in multiple sclerosis is developmentally immature. *J. Clin. Invest. 94*, 146–154.
34. Moscarello, M. A., Mastronardi, F. G., and Wood, D. D. (2007) The role of citrullinated proteins suggests a novel mechanism in the pathogenesis of multiple sclerosis. *Neurochem. Res. 32*, 251–256.
35. Musse, A. A., Boggs, J. M., and Harauz, G. (2006) Deimination of membrane-bound myelin basic protein in multiple sclerosis exposes an immunodominant epitope. *Proc. Natl. Acad. Sci. U.S.A. 103*, 4422–4427.
36. Sospedra, M., and Martin, R. (2005) Immunology of multiple sclerosis. *Annu. Rev. Immunol. 23*, 683–747.
37. Bates, I. R., Libich, D. S., Wood, D. D., Moscarello, M. A., and Harauz, G. (2002) An Arg/Lys → Gln mutant of recombinant murine myelin basic protein as a mimic of the deiminated form implicated in multiple sclerosis. *Protein Expression Purif. 25*, 330–341.
38. Hubbell, W. L., and Altenbach, C. (1994) Investigation of structure and dynamics in membrane proteins using site-directed spin labeling. *Curr. Opin. Struct. Biol. 4*, 566–573.
39. Hubbell, W. L., Mchaourab, H. S., Altenbach, C., and Lietzow, M. A. (1996) Watching proteins move using site-directed spin labeling. *Structure 4*, 779–783.
40. Fanucci, G. E., and Cafiso, D. S. (2006) Recent advances and applications of site-directed spin labeling. *Curr. Opin. Struct. Biol. 16*, 644–653.
41. Oh, K. J., Altenbach, C., Collier, R. J., and Hubbell, W. L. (2000) Site-directed spin labeling of proteins. Applications to diphtheria toxin. *Methods Mol. Biol. 145*, 147–169.
42. Bates, I. R., Matharu, P., Ishiyama, N., Rochon, D., Wood, D. D., Polverini, E., Moscarello, M. A., Viner, N. J., and Harauz, G. (2000) Characterization of a recombinant murine 18.5-kDa myelin basic protein. *Protein Expression Purif. 20*, 285–299.
43. Bates, I. R., Boggs, J. M., Feix, J. B., and Harauz, G. (2003) Membrane-anchoring and charge effects in the interaction of myelin basic protein with lipid bilayers studied by site-directed spin labeling. *J. Biol. Chem. 278*, 29041–29047.
44. Inouye, H., and Kirschner, D. A. (1988) Membrane interactions in nerve myelin: II. Determination of surface charge from biochemical data. *Biophys. J. 53*, 247–260.
45. Jo, E., and Boggs, J. M. (1995) Aggregation of acidic lipid vesicles by myelin basic protein: Dependence on potassium concentration. *Biochemistry 34*, 13705–13716.
46. Altenbach, C., Greenhalgh, D. A., Khorana, H. G., and Hubbell, W. L. (1994) A collision gradient method to determine the immersion depth of nitroxides in lipid bilayers: Application to spin-labeled mutants of bacteriorhodopsin. *Proc. Natl. Acad. Sci. U.S.A. 91*, 1667–1671.
47. Frazier, A. A., Wisner, M. A., Malmberg, N. J., Victor, K. G., Fanucci, G. E., Nalefski, E. A., Falke, J. J., and Cafiso, D. S. (2002) Membrane orientation and position of the C2 domain from cPLA2 by site-directed spin labeling. *Biochemistry 41*, 6282–6292.
48. Smith, P. K., Krohn, R. I., Hermanson, G. T., Mallia, A. K., Gartner, F. H., Provenzano, M. D., Fujimoto, E. K., Goeke, N. M., Olson, B. J., and Klenk, D. C. (1985) Measurement of protein using bicinchoninic acid. *Anal. Biochem. 150*, 76–85.
49. Peterson, G. L. (1977) A simplification of the protein assay method of Lowry et al. which is more generally applicable. *Anal. Biochem. 83*, 346–356.
50. Kabsch, W., and Sander, C. (1983) Dictionary of protein secondary structure: Pattern recognition of hydrogen-bonded and geometrical features. *Biopolymers 22*, 2577–2637.
51. Min, Y., Kristiansen, K., Boggs, J. M., Husted, C., Zasadzinski, J. A., and Israelachvili, J. (2009) Interaction forces and adhesion of supported myelin lipid bilayers modulated by myelin basic protein. *Proc. Natl. Acad. Sci. U.S.A. 106*, 3154–3159.
52. Qin, Z., Wertz, S. L., Jacob, J., Savino, Y., and Cafiso, D. S. (1996) Defining protein-protein interactions using site-directed spin-labeling: The binding of protein kinase C substrates to calmodulin. *Biochemistry 35*, 13272–13276.
53. Mchaourab, H. S., Lietzow, M. A., Hideg, K., and Hubbell, W. L. (1996) Motion of spin-labeled side chains in T4 lysozyme. Correlation with protein structure and dynamics. *Biochemistry 35*, 7692–7704.
54. Cajal, Y., Boggs, J. M., and Jain, M. K. (1997) Salt-triggered intermembrane exchange of phospholipids and hemifusion by myelin basic protein. *Biochemistry 36*, 2566–2576.
55. Bessonov, K., Bamm, V. V., and Harauz, G. (2010) Misincorporation of the proline homologue Aze (azetidine-2-carboxylic acid) into recombinant myelin basic protein. *Phytochemistry 71*, 502–507.
56. Deber, C. M., Moscarello, M. A., and Wood, D. D. (1978) Conformational studies on ^{13}C-enriched human and bovine myelin basic protein, in solution and incorporated into liposomes. *Biochemistry 17*, 898–903.
57. Libich, D. S., and Harauz, G. (2002) Interactions of the 18.5 kDa isoform of myelin basic protein with Ca^{2+}-calmodulin: *In vitro* studies using gel shift assays. *Mol. Cell. Biochem. 241*, 45–52.
58. Libich, D. S., and Harauz, G. (2002) Interactions of the 18.5 kDa isoform of myelin basic protein with Ca^{2+}-calmodulin: *In vitro* studies using fluorescence microscopy and spectroscopy. *Biochem. Cell Biol. 80*, 395–406.
59. Libich, D. S., Hill, C. M. D., Haines, J. D., and Harauz, G. (2003) Myelin basic protein has multiple calmodulin-binding sites. *Biochem. Biophys. Res. Commun. 308*, 313–319.
60. Majava, V., Wang, C., Myllykoski, M., Kangas, S. M., Kang, S. U., Hayashi, K., Baumgärtel, P., Heape, A. M., Lubec, G., and Kursula, P. (2010) Structural analysis of the complex between calmodulin and full-length myelin basic protein, an intrinsically disordered molecule. *Amino Acids 39*, 59–71.
61. Polverini, E., Boggs, J. M., Bates, I. R., Harauz, G., and Cavatorta, P. (2004) Electron paramagnetic resonance spectroscopy and molecular modelling of the interaction of myelin basic protein (MBP) with calmodulin (CaM): Diversity and conformational adaptability of MBP CaM-targets. *J. Struct. Biol. 148*, 353–369.
62. Majava, V., Petoukhov, M. V., Hayashi, N., Pirila, P., Svergun, D. I., and Kursula, P. (2008) Interaction between the C-terminal region of human myelin basic protein and calmodulin: Analysis of complex formation and solution structure. *BMC Struct. Biol. 8*, 10.
63. Polverini, E. (2008) Molecular modelling of the interaction of myelin basic protein peptides with signalling proteins and effects of post-translational modifications. In Myelin Basic Protein (Boggs, J. M., Ed.) pp 169−195, Nova Science Publishers, New York.
64. Cornette, J. L., Cease, K. B., Margalit, H., Spouge, J. L., Berzofsky, J. A., and DeLisi, C. (1987) Hydrophobicity scales and computational techniques for detecting amphipathic structures in proteins. *J. Mol. Biol. 195*, 659–685.